Coherent-Precipitation-Stabilized Phase Formation in Over-stoichiometric Rocksalt-Type Li Superionic Conductors

Yu Chen†, Xinye Zhao†, Ke Chen, Krishna Prasad Koirala, Raynald Giovine, Xiaochen Yang, Shilong Wang, Nathan J. Szymanski, Shuoyan Xiong, Zhengyan Lun, Huiwen Ji, Chongmin Wang, Jianming Bai, Feng Wang, Bin Ouyang, Gerbrand Ceder**

† Equal contributions

Y. Chen, X. Zhao, X. Yang, S. Wang, N. J. Szymanski, G. Ceder
Department of Materials Science and Engineering
University of California, Berkeley
Berkeley, CA 94720, USA
Email: gceder@berkeley.edu

Y. Chen, X. Zhao, X. Yang, S. Wang, N. J. Szymanski, G. Ceder
Materials Sciences Division
Lawrence Berkeley National Laboratory
Berkeley, CA 94720, USA

K. Chen, J. Bai
Brookhaven National Laboratory
Upton, NY 11973, USA

K. P. Koirala
Physical and Computational Sciences Directorate
Pacific Northwest National Laboratory
Richland, WA 99354, USA

R. Giovine, S. Xiong
College of Chemistry
University of California Berkeley
Berkeley, CA 94720, USA

Z. Lun
School of Chemical Sciences
University of Chinese Academy of Sciences
Beijing 100049, China

H. Ji
Department of Materials Science and Engineering
University of Utah
Salt Lake City, UT 84112, USA

C. Wang
Environmental Molecular Sciences Laboratory
Pacific Northwest National Laboratory

Richland, WA 99354, USA

F. Wang
Applied Materials Division
Argonne National Laboratory
Argonne, IL 60439, USA

B. Ouyang
Department of Chemistry and Biochemistry
Florida State University
Tallahassee, FL 32306, USA
Email: bouyang@fsu.edu

Keywords: Coherent precipitation, over-stoichiometric rocksalt, Li superionic conductivity, face-sharing configurations, synthesis science

Abstract

Rationalizing synthetic pathways is crucial for material design and property optimization, especially for polymorphic and metastable phases. Over-stoichiometric rocksalt (ORX) compounds, characterized by their face-sharing configurations, are a promising group of materials with unique properties; however, their development is significantly hindered by challenges in synthesizability. Here, taking the recently identified Li superionic conductor, over-stoichiometric rocksalt Li–In–Sn–O (o-LISO) material as a prototypical ORX compound, we systematically investigate the mechanisms of phase formation. We reveal that the spinel-like phase with unconventional stoichiometry forms as coherent precipitate from the high-temperature-stabilized cation-disordered rocksalt phase upon fast cooling. This process prevents direct phase decomposition and kinetically locks the system in a metastable state with the desired face-sharing Li configurations. This insight enables us to enhance the ionic conductivity of o-LISO to be > 1 mS cm^{-1} at room temperature through low-temperature post-annealing. Our work offers insights into the synthesis of ORX materials and highlights important opportunities in this new class of materials.

Although synthesis is generally the first step in material exploration, it is by no means a trivial task to optimize the microstructure of multi-phase samples for a particular property. This is particularly challenging when some target phases are metastable and requires a careful understanding of the thermodynamic driving forces and kinetic pathways[1]. Recent advancements in in situ observation techniques for material synthesis, coupled with ab initio calculations, have significantly improved our understanding of how synthesis parameters influence reactions, allowing for the exploration of non-equilibrium phase-formation pathways, and leading to more synthetic control of local structures and subsequent material performance[1-9].

Lithium-metal oxides with a face-centered cubic (*fcc*) anion framework are widely used as battery materials, especially the compositions with cation/anion ratios equal to 1 (e.g., layered[10], rocksalt[11]) or less than 1 (e.g., spinel[12-13]). Over-stoichiometric rocksalt (ORX) materials in which the cation/anion ratio is greater than 1 are less well studied despite them having the potential to promote fast Li-ion transport or enhanced electrochemical capacity when Li is "stuffed" into tetrahedral (Tet)−octahedral (Oct) face-sharing arrangements[14-15]. This sparsity mainly stems from the synthetic difficulties associated with ORX materials, as cation over-stoichiometry requires some degree of Tet−Oct face-sharing occupancy, which increases the energy of the structure due to the electrostatic repulsion of cations in this close proximity. Indeed, most of the small number of reported ORX materials (e.g., $Li_{3+x}V_2O_5$[14], $Li_{7+x}Ti_5O_{12}$[16]) have been obtained only by electrochemically over-lithiating stoichiometric rocksalt compounds.

Recently, an ORX compound, $Li_{17}In_9SnO_{24}$ (o-LISO), was reported to exhibit a high Li-ion conductivity (3.4×10^{-4} S cm^{-1} at room temperature) owing to the face-sharing Li configurations induced by Li over-stoichiometry[17]. This ORX material can be directly synthesized using conventional solid-state methods, highlighting ORX as a new group of promising candidates to be

explored as solid-state electrolytes. Our previous study on o-LISO showed that with Li over-stoichiometry (which results in a cation/anion ratio >1), a spinel-like phase with Li partial 8a site occupancy and full 16c site occupancy (denoted as the "s-phase") forms as nanosized domains within the disordered rocksalt (DRX) matrix. However, it remains unclear why the s-phase forms in o-LISO and why it only forms as nanosized domains. Understanding the formation mechanism of the highly ionically conductive s-phase in the ORX system is vital for further optimization and design of ORX-based Li superionic conductors. Furthermore, this knowledge can serve as a guideline for understanding how face-sharing configurations can be synthesized and stabilized in ORX materials.

In this work, we systematically explore the non-equilibrium formation pathways in a prototypical ORX compound, o-LISO, using ex situ and in situ synchrotron X-ray diffraction (XRD). The work is complemented by an investigation of the thermodynamic landscape using ab initio calculations. Our findings indicate that the s-phase is a thermodynamically metastable yet kinetically favorable phase, forming as coherent precipitates from the over-stoichiometric DRX (o-DRX) phase during fast cooling. The coherent precipitate s-phase prevents the direct phase decomposition into the equilibrium phases and conserves the face-sharing configuration in o-LISO. Armed with an understanding of the synthesis mechanism, we further improve the ionic conductivity of o-LISO to 1.45 mS cm^{-1} by applying a low-temperature post-annealing treatment.

In situ experimental study of o-LISO synthesis

The synthesis of o-LISO was conducted by a conventional solid-state method. Figure 1a presents the XRD patterns of o-LISO calcined at 1050 °C and followed by different cooling processes. When the sample is air quenched from 1050 °C, the XRD pattern shows peaks corresponding to the s-phase (purple vertical ticks) and o-DRX (green ticks), whereas when the sample is slowly cooled at 5 °C/min, XRD peaks of $LiInO_2$-type ('γ', grey ticks) and Li_3InO_3-like ('r', red ticks) phases emerge instead. While the s-phase and o-DRX have desired face-sharing Li configurations that can promote fast Li-ion conduction[17], the 'γ' and 'r' phases do not possess such face-sharing configurations: the 'γ' phase has a stoichiometric rocksalt composition, and the 'r' phase orders Li into edge-sharing Tet dumbbell layers to accommodate a higher Li content than the o-LISO composition. The formation of the 'γ' and 'r' phases is thus regarded as phase decomposition, which leads to a very low Li-ion conductivity below the detectable limit (Figure S1).

To understand the phase formation of o-LISO, we performed in situ synchrotron XRD to monitor the phase evolution during a typical synthesis experiment: the ball-milled precursors were heated to 1050 °C at heating rates of 20 °C min^{-1} (< 600 °C) and 10 °C min^{-1} (> 600 °C), then held at 1050 °C for 1 h, and subsequently cooled down at a rate of 100 °C min^{-1} to mimic the quenching process. Further details are provided in Methods. The resulting XRD patterns are presented in Figure 1b as an intensity plot as function of temperature. In the low-temperature XRD scans that are performed at the beginning of the in situ experiment, only the precursors In_2O_3 and SnO_2 are observed. The precursor Li_2CO_3 is not visible as it amorphizes during ball-milling. Upon heating, the precursors remain unreacted until 670 °C when Li_2CO_3 and In_2O_3 first react to form the 'γ' phase. At approximately 770 °C, Li_2SnO_3 peaks can be identified, indicating reaction

between the Li source and SnO_2. The peaks associated with the precursors completely disappear at 800 °C. At approximately 900 °C, Li_2SnO_3 disappears, leaving 'γ' as the only crystalline phase present. This suggests that Sn^{4+} is incorporated into the 'γ' phase. The 'γ' phase then transforms into DRX and the 'r' phase upon further ramping above 950 °C. As Li_2CO_3 is hard to observe in XRD after ball-milling, we further applied thermogravimetric analysis (TGA) and differential scanning calorimetry (DSC) to monitor the heating process (Figure S2). The results reveal that Li_2CO_3 melts at around 720 °C and continues to decompose into Li_2O and CO_2 from 570 °C to 930 °C. This observation indicates that Li_2CO_3 fully reacts by 930 °C, which is close to the temperature where 'γ' transforms into the DRX and 'r' phase mixture. This suggests that the 'γ' phase observed during heating does not contain the intended over-stoichiometric Li content, as the consumption of all the Li precursor closely coincides with the DRX and 'r' phase formation.

While the temperature is maintained at 1050 °C, the DRX peaks remain unchanged whereas the peak intensities of the 'r' phase gradually decrease (Figures 1b, d). Given its high Li content, the disappearance of the 'r' phase is likely due to Li loss through evaporation of the volatile Li_2O, as discussed in previous work[17]. After 1 h, the 'r' phase completely disappears, resulting in a pure DRX phase. We identify the DRX phase here as over-stoichiometric, as no other phases were identified to account for the Li over-stoichiometry, and refer to it as o-DRX. Upon fast cooling (100 °C/min), the diffraction peaks of the s-phase start to appear at around 950 °C, as shown in Figure 1c, and these peak intensities increase upon further cooling to 850 °C. Further cooling does not change the XRD patterns. The final products, s-phase and o-DRX, are consistent with those obtained from a typical air-quenched ex situ synthesis (Figure 1a). Since our previous study demonstrated that the s-phase will not form if the composition is near stoichiometric[17], we presume the composition is still over-stoichiometric despite some Li loss during heating. The

evolution of the observed phase weight fractions during the entire in situ XRD experiment is summarized in Figure 1d. We can conclude that o-DRX is the high-temperature-stabilized phase and that the s-phase forms upon fast cooling of o-DRX.

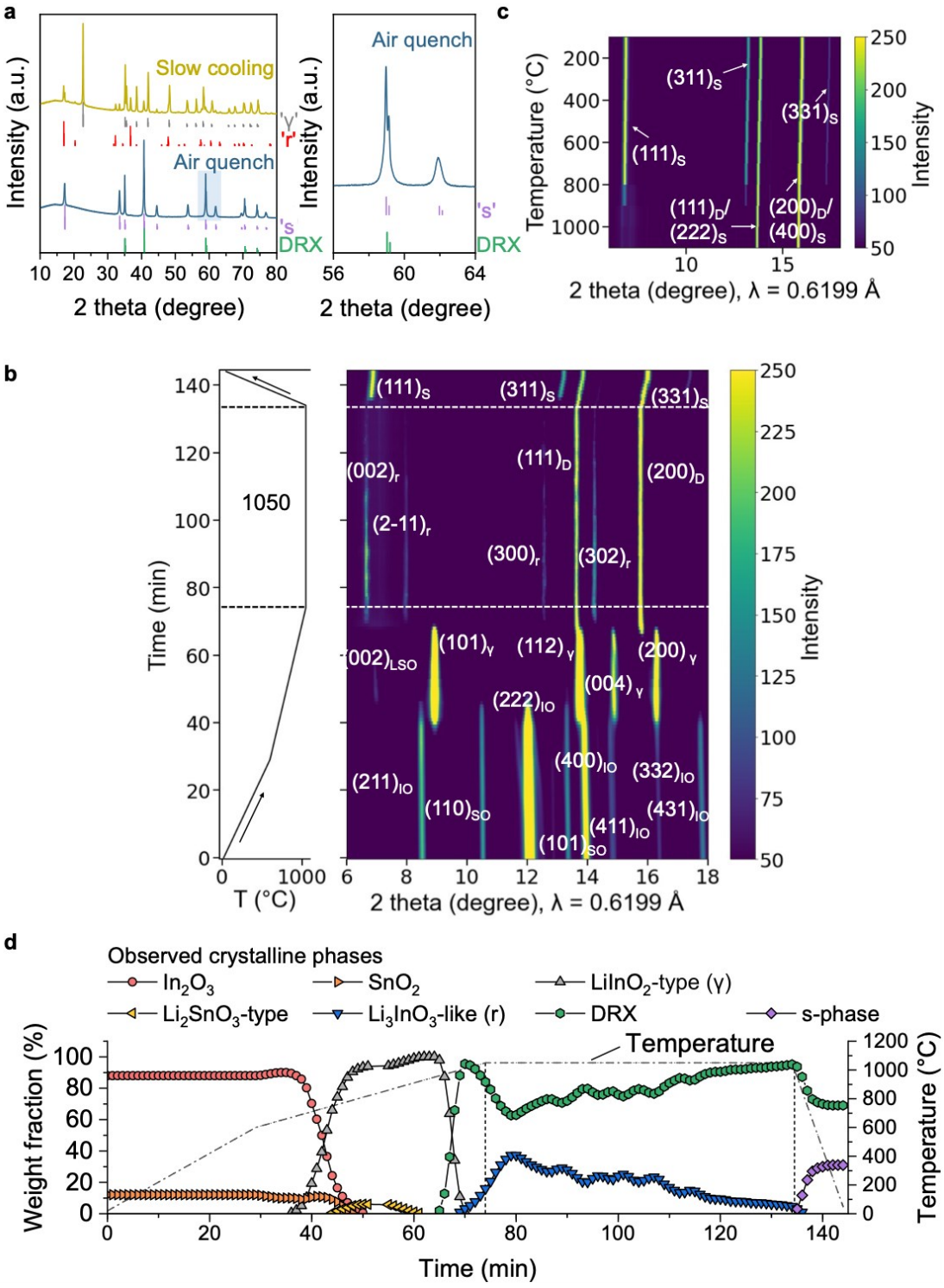

Figure 1. Reaction pathways in the solid-state synthesis of o-LISO. (a) Room-temperature ex situ XRD patterns of o-LISO synthesized at 1050 °C, followed by air quenching or slow cooling (5 °C/min). The subplot on the right shows an enlarged XRD pattern of air-quenched o-LISO, corresponding to the blue-shaded region in the figure on the left. The Bragg positions of the identified phases are labelled by vertical tick marks: purple–s-phase, green–DRX, grey–$LiInO_2$-type ('γ') phase, red–Li_3InO_3-like ('r') phase. **(b)** Intensity plot of in situ synchrotron XRD highlighting the evolution of the Bragg peaks. The heating profile is shown in the left panel. The abbreviations used for the phases are: In_2O_3–IO, SnO_2–SO, $LiInO_2$-type–γ, Li_3InO_3-like–r, DRX–D, s-phase–S. **(c)** Expanded intensity plot of in situ synchrotron XRD upon fast cooling. **(d)** Evolution of the weight fractions of the observed crystalline phases obtained from the in situ synchrotron XRD patterns. The color schemes are: In_2O_3–red, SnO_2–orange, Li_2SnO_3-type–yellow, $LiInO_2$-type–grey, Li_3InO_3-like–blue, DRX–green, s-phase–purple.

Effects of fast-cooling rate on s-phase formation

The fact that the s-phase forms upon fast cooling motivated us to further investigate the effect of the cooling rate on s-phase formation. A water quench was performed to achieve a faster cooling rate than the air quench. Figure 2a presents the XRD patterns of water-quenched o-LISO (denoted as "WQ-o-LISO") and air-quenched o-LISO (denoted as "AQ-o-LISO"), which were obtained using exactly the same synthesis procedure except for the cooling step. The diffraction patterns of the o-DRX phase are similar, whereas the peaks of the s-phase are broader with lower intensity for WQ-o-LISO as compared to AQ-o-LISO. These results suggests that water quenching leads to a s-phase with lower phase fraction and/or smaller domain size. Liquid nitrogen quench was also attempted, resulting in a slightly lower but comparable s-phase fraction to that of water quench, as

shown in Figure S3. These results are consistent with a nucleation and growth mechanism[18] for the formation of the s-phase. As higher undercooling increases the driving force for nucleation but slows down the growth, the more rapid temperature decrease during water quench or liquid nitrogen quench should lead to more nuclei of s-phase which have had less time to grow.

^{6}Li solid-state nuclear magnetic resonance (ssNMR) was applied to probe the Li local environments in the air-quenched and water-quenched o-LISO, with the results shown in Figure 2b. The ^{6}Li ssNMR spectra consist of two main resonances, a sharp one near 0 ppm attributed to Oct Li, and a broader one near 7 ppm that reflects Tet Li[17]. Comparing to AQ-o-LISO, the broad signal in the spectrum of WQ-o-LISO has a much lower intensity and its chemical shift decreases from 7.6 to 6.6 ppm, while the sharp signal remains similar, at approximately 0.8 ppm. Each Li environment (i.e., Tet and Oct Li) requires a two-component model to reliably fit the observed line shape of each signal (see Table S1 for more details). The difference in intensity and chemical shift of the broad signal between WQ-o-LISO and AQ-o-LISO is attributed to the slight variation in the local environment for Li in different Tet or Oct sites in o-DRX and the s-phase. The fitting results are presented in Figure 2b and Table S1. We find that the component at 9.5 ppm (purple shading) decreases dramatically in WQ-o-LISO compared to AQ-o-LISO, whereas the component at 6.3 ppm (green shading) remains similar. Since the XRD results indicate that WQ-o-LISO has a lower s-phase fraction than AQ-o-LISO (Figure 2a), we attribute the component at 9.5 ppm (purple shading) to the Tet Li in the s-phase.

Electrochemical impedance spectroscopy (EIS) was applied to measure ionic conductivities of WQ-o-LISO and AQ-o-LISO at room-temperature (RT), with the resulting Nyquist plots shown in Figure 2c. The measured total Li-ion conductivity of WQ-o-LISO is 7.96×10^{-5} S cm^{-1}, which is lower than that of AQ-o-LISO (4.09×10^{-4} S cm^{-1}). This result is consistent with our previous

finding[17] that the s-phase exhibits higher Li-ion conductivity than o-DRX because of its 3D connected Tet–Oct face-sharing Li polyhedral network.

Based on the above in situ and ex situ experiments, we attain a more complete picture of the phase-formation pathways in the synthesis of o-LISO, as summarized in Figure 2d. Unlike a typical solid-state reaction in which different phases are stabilized and form at specific temperature ranges during heating, in o-LISO, the s-phase does not appear during the heating process but only forms upon fast cooling of o-DRX, the high-temperature-stabilized phase. Our finding reveals that the cooling rate plays a crucial role in s-phase formation: upon slow cooling (e.g., natural cooling), the o-DRX phase directly decomposes into the 'γ' and 'r' phases; whereas if cooling is too fast, there is not much time for the s-phase to nucleate and grow. Thus, an appropriate cooling rate is required to achieve a relatively high s-phase fraction while avoiding phase decomposition into the 'γ' and 'r' phases.

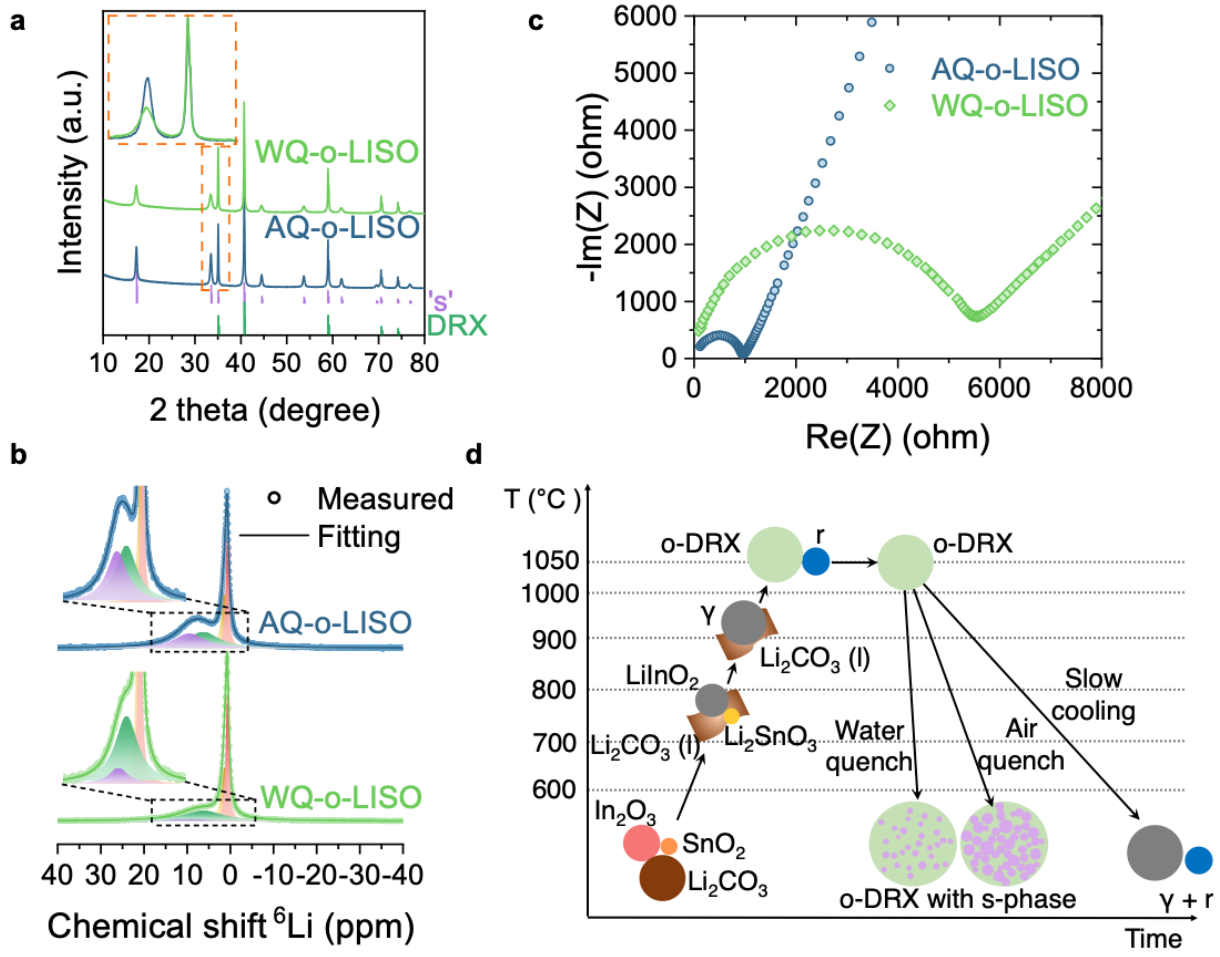

Figure 2. Comparison of water-quenched and air-quenched o-LISO. (a) XRD patterns of o-LISO synthesized at 1050 °C, followed by air or water quenching. **(b)** ^{6}Li magic-angle spinning (MAS) ssNMR spectra of air or water quenched o-LISO. The fitting components are shown in colored shadings. **(c)** Nyquist plots of air- or water-quenched o-LISO from EIS measurement at RT. **(d)** Schematic illustration of phase-formation pathways in the solid-state synthesis of o-LISO with variable cooling rates.

Thermodynamic stability of Li–In–Sn–O system with Li over-stoichiometry

The complex phase evolution of o-LISO during heating and cooling motivated us to explore the specific thermodynamic landscape and to develop generalizable guidelines for synthesizing compositions within the Li–In–Sn–O (LISO) chemical space with Li over-stoichiometry. To evaluate the relative thermodynamic stability of different phases observed in the in situ experiments, we performed a set of density-functional theory (DFT) calculations on 39 LISO compositions. For each composition, we calculated the energies of the s-phase, o-DRX, over-stoichiometric $LiInO_2$-type ('γ'), and Li_3InO_3-like ('r') phases. The specific cation arrangements are shown in Figure 3a for the s-phase and o-DRX (based on the refined structures from the previous study[17]) as well as in Figure S4 for the 'γ' and 'r' phases. For each prototype phase, we created 10 configurations with low electrostatic energy and used them as input for DFT calculations[19]. More computational details are provided in the Methods section.

We evaluate the thermodynamic stability of the s-phase at both 0 K and the synthesis temperature (1323 K), (Figure 3b left and right, respectively) by calculating free energy above the global hull for the s-phase at different compositions. Competing phases are taken as all phases in the relevant composition space present in the Materials Project (MP)-database[20-22]. Possible competing phases for these s-phase compositions include ordered $LiInO_2$ ('γ'), Li_3InO_3 ('r'), Li_2O, Li_2SnO_3, and Li_8SnO_6. The results are presented in the ternary diagrams in Figure 3b. It is noted that all our considered LISO compositions can be numerically represented by a linear combination of $LiInO_2$, Li_2SnO_3, and Li_2O, each normalized to a per-atom basis. In particular, the Li-excess level (Li substitution on the Oct In^{3+}/Sn^{4+} sites) increases with both $x Li_2SnO_3$ and $y Li_2O$, and the Li over-stoichiometric level (making the overall cation/anion ratio larger than 1) only increases with $y Li_2O$. Colors towards the darker-green end represent a more positive $E_{\mathrm{hull}}^{\mathrm{s}}$ (eV/O_4),

indicating that the s-phase at the corresponding compositions is less stable. The white color represents a global hull energy below or equal to 0 eV/O_4 and indicates that the s-phase is stable. Figure 3b (left) shows that higher Sn content (toward higher $x$$Li_2SnO_3$) tends to destabilize the s-phase, which is consistent with experimental observations (Figure S5). The effect of the Li over-stoichiometric level is slightly more complex, as the s-phase becomes more stable when $y$$Li_2O$ increases from 0 to 0.167, but is destabilized when $y$$Li_2O$ further increases from 0.167 to 0.333. This may be explained by competing forces: Introduction of over-stoichiometric Li brings the system closer to the stoichiometry of the overlithiated $Li^{8a}(Li^{16c})_2(M^{16d})_2O_4$ spinel. This s-phase ordering avoids face-sharing configurations between Li and high-valent cations. For $y$$Li_2O$ < 0.167, the 8a site occupancy of the s-phase is < 0.5, ensuring that each occupied 16c site only face-shares with a single occupied Tet site. However, when more Li over-stoichiometry is introduced such that Occ(Li_{8a}) > 0.5 or $y$$Li_2O$ > 0.167, some of the Oct Li at the 16c site will have to face share with two Tet 8a Li simultaneously, which significantly increases the electrostatic repulsion and destabilizes the s-phase. At T = 0 K, we predict that the most stable LISO composition with both Li-excess and Li over-stoichiometry is $Li_{29}In_{21}SnO_{48}$ with an $E_{\mathrm{hull}}^{\mathrm{s}}$ = 0.15 eV/O_4. Thus, the s-phase is not the ground state for any of our calculated compositions.

To estimate the E_{hull}^{s} at non-zero temperature, we calculated the entropy of ideal mixing, normalized per-O_4, based on the Li/vacancy disorder on the 8a site and the Li/In/Sn disorder on the 16d site. The details are provided in the Methods section. This can be considered as an upper bound of the configurational entropy. At a synthesis temperature of T = 1323 K, the entropic contribution stabilizes the s-phase (the colors shift to white and the blue end) at all the considered compositions, as shown in Figure 3b (right). The predicted most stable s-phase composition at 1323 K is $Li_{31}In_{15}Sn_5O_{48}$ with an E_{hull}^{s} = –0.02 eV/O_4. Notice that the experimental composition

$Li_{17}In_9SnO_{24}$ also receives a large entropic stabilization from $E_{\text{hull}}^{\text{S}}$ = 0.33 eV/O_4 at 0 K to 0.16 eV/O_4 at 1323 K.

To understand the phase transition upon fast cooling, we compare the relative stability of the s-phase and o-DRX, namely $E^{\text{S}} - E^{\text{D}}$, for each composition at both 0 K and 1323 K, as shown in the left and right part of Figure 3c. From Figure 3c (left), the predominant blue color indicates that the s-phase is more stable than the o-DRX phase at low temperature for most of the calculated compositions. In comparison, at 1323 K (Figure 3c (right)), o-DRX is more stable as indicated by the predominantly white and green color. For example, for $Li_{17}In_9SnO_{24}$ (yellow circle), $E^{\text{S}} - E^{\text{D}}$ is calculated to be –0.35 eV/O_4 at 0 K, but +0.07 eV/O_4 at 1323 K. The effect of temperature in stabilizing o-DRX is expected as all Oct and Tet cation sites in the o-DRX structure contribute to disorder (Figure 3a). In comparison for s-phase, only half of the Oct cation sites, i.e., the 16d sites, participate in the disorder, while the other half (16c) are fully occupied by Li and show no disorder. Thus o-DRX gains larger entropic stabilization than the s-phase at high temperatures. At both temperatures, a high Li over-stoichiometry level ($y$$Li_2O$ > 0.167) destabilizes the s-phase significantly as more than half of the 8a sites are occupied, which is consistent with our findings in Figure 3b. Based on the results in Figure 3c, the s-phase to o-DRX transition temperature ($T^{\text{S}\rightarrow\text{D}}$) for all the considered compositions is plotted in Figure 3d. Here, colors toward the red end of the rainbow spectrum indicate a higher $T^{\text{S}\rightarrow\text{D}}$, and vice versa for colors toward the blue end. Consistent with the results in Figure 3c, $T^{\text{S}\rightarrow\text{D}}$ increases with the relative stability of the s-phase. For certain composition with $y$$Li_2O$ close to 0.333, we may see a $T^{\text{S}\rightarrow\text{D}}$ = 0 K, indicating that the s-phase is less stable than o-DRX at all temperature. The predicted $T^{\text{S}\rightarrow\text{D}}$ for $Li_{17}In_9SnO_{24}$ is 1089 K, which is close to the experimentally observed transition-temperature range of 1123–1223 K.

A similar analysis was performed to evaluate the relative stability of the s-phase with respect to the 'γ' and 'r' phases at the same compositions. As shown in Figure S6a, the s-phase is slightly more stable over the 'γ' phase when $y\mathrm{Li_2O} < 0.167$ at both 0 K and 1323 K. Lower temperature tends to stabilize the s-phase more relative to the 'γ' phase; however, at identical compositions, the relative energy difference between 'γ' and s-phase is lower compared to the energy difference between the o-DRX and s-phase. As shown in Figure S6b, at 0 K, the s-phase tends to be more stable than the 'r' phase when $y\mathrm{Li_2O} < 0.167$; however, once more than half of the 8a site is occupied ($y\mathrm{Li_2O} > 0.167$), the 'r' phase becomes the more stable phase. This is expected as the dumbbell-like edge-sharing Tet Li configuration in the 'r' phase reduces the large electrostatic repulsion of the face-sharing configuration seen in the s-phase, and thus can better accommodate a high Li over-stoichiometry level. At 1323 K, the s-phase is less stable than the 'r' phase for most calculated compositions. It is important to recognize that here, we compare phase stabilities for phases at the same compositions so that we can understand which structures can transform into each other without long-range diffusion. Nonetheless, global equilibrium, as expressed by the convex hull calculations shown in Figure 3b, also allows for separation into the 'γ' and 'r' phases with different compositions.

Our results indicate that the s-phase is generally not the global ground state. However, with a low-to-intermediate Li over-stoichiometry level ($0.050 < y\mathrm{Li_2O} < 0.167$), the s-phase is the most stable ordering among all the considered single-phase solutions at low temperature. Yet, the o-DRX phase gains the most entropic stabilization due to its high level of cation disorder, making it the high-temperature phase, as observed in the experiments. In addition, a high Li over-stoichiometry level ($y\mathrm{Li_2O} > 0.167$) creates an electrostatically unstable configuration in the s-

phase in which one Oct 16c Li face-shares with two Tet 8a Li simultaneously. Such configuration destabilizes s-phase and favors ‘r’ phase formation.

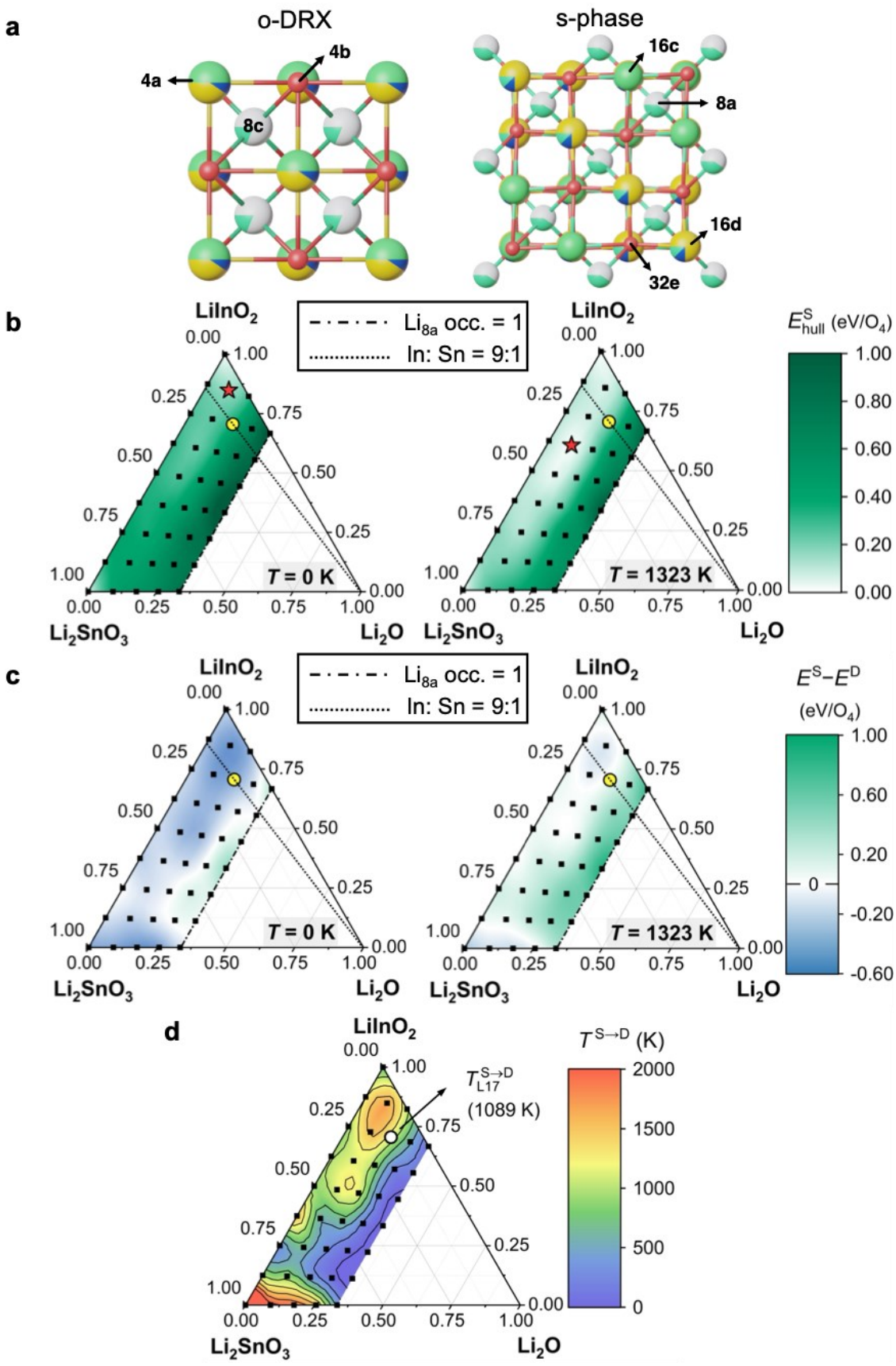
a
o-DRX
4a
4b
8c
s-phase
16c
8a
16d
32e
b
LiInO2
Li8a occ. = 1
In: Sn = 9:1
T = 0 K
T = 1323 K
Li2SnO3
Li2O
E^S_hull (eV/O4)
c
E^S−E^D (eV/O4)
d
T^S→D (K)
T^S→D_L17 (1089 K)

Figure 3. Computed and interpolated stabilities of over-stoichiometric Li–In–Sn–O compounds with s-phase ('S') and o-DRX ('D') ordering. (a) Schematic crystal structures of o-DRX (left) and s-phase (right) with Li over-stoichiometry, visualized perpendicular to the (100) plane. The green, yellow, blue, and red spheres represent Li, In, Sn, and O, respectively. Mixed colors indicate mixed or partial occupancy. **(b)** Calculated energy above hull of the s-phase structure for 39 LISO compositions at 0 K (left) and 1323 K (right). The hull is the lowest DFT-computed energy, normalized on a per O_4 basis, of all the competing phases or their linear combinations. The white color denotes $E^{s}_{\text{hull}} \leq 0$ eV/O_4, whereas colors towards the green end represent a more positive E^{s}_{hull}. The yellow circle symbol denotes $Li_{17}In_9SnO_{24}$, the experimentally synthesized composition. The red star denotes the LISO composition with the most stable s-phase, $Li_{29}In_{21}SnO_{48}$ at 0 K and $Li_{31}In_{15}Sn_5O_{48}$ at 1323 K. The dash-dotted line indicates a $y$$Li_2O$ of 0.333, which corresponds to a Li_{8a} occupancy of 1. The LISO compositions on the dotted line have an In:Sn ratio of 9:1. **(c)** Computed energy stability of s-phase relative to o-DRX at 0 K (left) and 1323 K (right). The energy is normalized per O_4. More negative $E^{S} - E^{D}$ values are represented by deeper blue colors, and more positive $E^{S} - E^{D}$ values are represented by deeper green colors. The white color denotes a relative energy difference of 0 eV/O_4. **(d)** Computed s-phase to o-DRX phase-transition-temperature map based on DFT energetics and configurational entropy of ideal mixing. Colors towards the red end of the rainbow spectrum indicate a higher transition temperature, and those towards the blue end indicate a lower transition temperature. The white circle symbol denotes the predicted $T^{S\rightarrow D}$ of $Li_{17}In_9SnO_{24}$, which is 1089 K. The contour lines connect compositions that share the same $T^{S\rightarrow D}$.

Kinetically favorable s-phase formation through coherent precipitation

Our experimental findings (Figs. 1-2) indicate that upon fast cooling, s-phase nucleates from o-DRX. Slow cooling, on the other hand, allows o-DRX to decompose into the equilibrium 'γ' and 'r' products. This cooling-dependent behavior suggests that s-phase formation from o-DRX may be kinetically favorable. Our previous study[17] showed that nanosized s-phase domains are dispersed in the o-DRX matrix, instead of separate s-phase and o-DRX particles[17]. To understand the relation between the s-phase and the parent o-DRX from which it forms we investigate their microstructure in more detail. Atomically resolved high-angle annular dark-field (HAADF)-scanning transmission electron microscopy (STEM) images were obtained for o-LISO (refers to air-quenched sample unless stated otherwise), as shown in Figure 4a. Figure 4b presents a magnified atomic-resolution HAADF image from the green rectangular area in Figure 4a, showing the o-DRX phase. This image is consistent with the fast Fourier transform (FFT) map showing the [110] diffraction pattern of a DRX structure (Figure 4c). For the purple rectangular area in Figure 4a, the magnified atomic-resolution HAADF image (Figure 4d) displays s-phase features with contrast between the 16d and 16c site, as the 16d site is mainly occupied by heavy atoms (e.g., In, Sn) while the 16c site is occupied by light Li. This is confirmed by the FFT image that can be indexed to a spinel-like structure along the [110] direction (Figure 4e). Therefore, the HAADF image clearly displays the concurrent presence of s-phase and o-DRX domains in a single particle along the same [110] direction, indicating that the two phases are orientationally aligned. Furthermore, as shown in Figure 4f which is the magnified HAADF image from the blue rectangular area in Figure 4a, there is no clear phase boundary between the s-phase and o-DRX regions. Instead, a continuous lattice between the two phases with coherent interfaces is observed. These results strongly suggest that the s-phase forms as coherent precipitates from o-DRX.

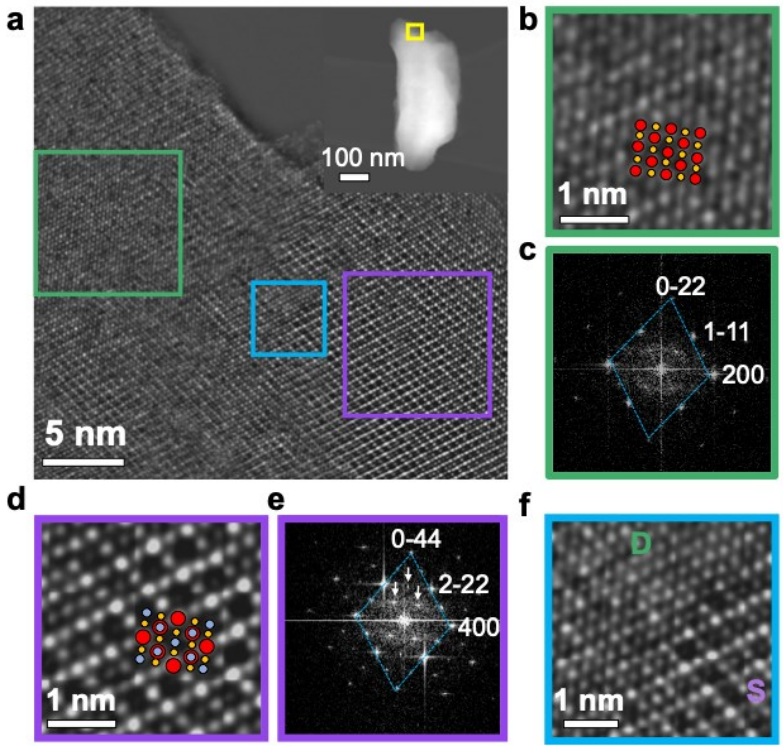

Figure 4. Atomic-resolution images of o-LISO. (a) Atomic-resolution HAADF-STEM image of o-LISO along the [110] zone axis. The inset shows the image of an o-LISO particle, and the yellow rectangle indicates the region from which the atomic-resolution image was taken. **(b)** Magnified image from the green rectangular area in (a), showing cation-disordered rocksalt ordering (red: metals at 4a site, yellow: O). **(c)** Corresponding FFT image of the green rectangular area in (a). **(d)** Magnified image from the purple rectangular area in (a), which exhibits a spinel-like ordering (red: metals at 16d site, blue: metals at 16c site, yellow: O). **(e)** Corresponding FFT image of the purple rectangular area in (a). The extra spots (marked by white arrows) are attributed to the spinel-like structure and are absent in (c). **(f)** Magnified image from the blue rectangular area in (a), showing a coherent interface between the s-phase and o-DRX phase.

Because o-DRX, s-phase and 'γ' phase all share a common close-packed *fcc* oxygen sublattice, s-phase and 'γ' phase can in principle both coherently precipitate from o-DRX. To better quantify this competition, we calculated the relative stability of the s-phase with respect to the 'γ' phase with and without the o-DRX lattice constraints to simulate coherent and incoherent precipitation, respectively. The two phases were compared at identical compositions. As shown in Figures 5a–b, for each considered composition (denoted with a black square symbol), a common supercell was selected for all three phases to ensure structural compatibility, and we enumerated 10 cation arrangements with low electrostatic energy for each phase. To create relevant constraints for the coherent precipitation in o-DRX, we determined the average o-DRX lattice parameter from the DFT-relaxed o-DRX configurations and used this lattice parameter to constrain the supercells of the s-phase and 'γ' phase structures. Internal coordinates were fully relaxed. Incoherent precipitation is approximated by fully relaxed s-phase and 'γ' phase energetics. In Figures 5a–b, a darker green color represents a more positive $E^S - E^\gamma$ (meV/atom), and a darker blue color represents a more negative $E^S - E^\gamma$. The incoherent precipitation case (Figure 5a) clearly favors the 'γ' phase at low Li over-stoichiometry levels below $y\mathrm{Li_2O} < 0.05$, consistent with the presence of 'γ' phase on the global convex hull. Conversely, with an increasing Li over-stoichiometry, the s-phase is predicted to be the more stable phase. When the structures of the s-phase and 'γ' phase are constrained by the o-DRX lattice, mimicking coherent precipitates, a distinct trend emerges. As shown in Figure 5b, the s-phase demonstrates enhanced stability compared to the 'γ' phase across all computed compositions. For example, for $\mathrm{Li_{17}In_9SnO_{24}}$, $E^S - E^\gamma$ in the coherent scenario is around –37 meV/atom, a substantial stabilization for s-phase as compared to –17 meV/atom in the incoherent case. Even for the exact $\mathrm{LiInO_2}$ composition without Li over-stoichiometry (top point in Figures 5a-b), $E^S - E^\gamma$ changes from +20 meV/atom in the incoherent scenario to only +5

meV/atom in the coherent construct, indicating a large stabilization of the s-phase from the lattice constraint. This finding suggests that the s-phase is more prone to forming coherent precipitates from the o-DRX structure, and the 'γ' phase can be significantly destabilized if it is confined to the o-DRX lattice.

The other possible phase-decomposition product, the 'r' phase, has a hexagonal closed-packed (*hcp*) anion sublattice rather than the *fcc* anion sublattice present in the 'γ', s-phase and o-DRX. This makes it unlikely that the 'r' phase would form coherent precipitates in o-DRX.

Based on classical nucleation theory[23], the nucleation barrier is proportional to the cube of the interfacial energy: $\Delta G^* = \frac{16\pi\gamma^3}{3\Delta G^2}$, where γ is the interfacial energy, ΔG is the bulk free energy change. Coherent precipitation tends to have a significantly lower interfacial energy than incoherent precipitation (0−200 mJ m^{-2} for coherent vs. 500−1000 mJ m^{-2} for incoherent)[24], resulting in a lower nucleation barrier. Thus, we expect that the coherent-precipitate s-phase has a much higher nucleation rate than the 'γ' and 'r' phases, which we believe to be the origin of the fast kinetics for s-phase formation. This is similar to the nanoscale stabilization of metastable phase in small particles as has been demonstrated in iron oxides[25-26]. As illustrated in Figure 5c, although the thermodynamic driving force for precipitation of the s-phase is lower than that for the phase decomposition into 'γ' and 'r' phases, the s-phase nucleates more rapidly because it can form as coherent precipitates from o-DRX. Upon fast cooling when the nucleation rate is limiting, the kinetically favorable s-phase forms; whereas upon slow cooling when there is enough time for nucleation, the thermodynamically favorable phase decomposition occurs.

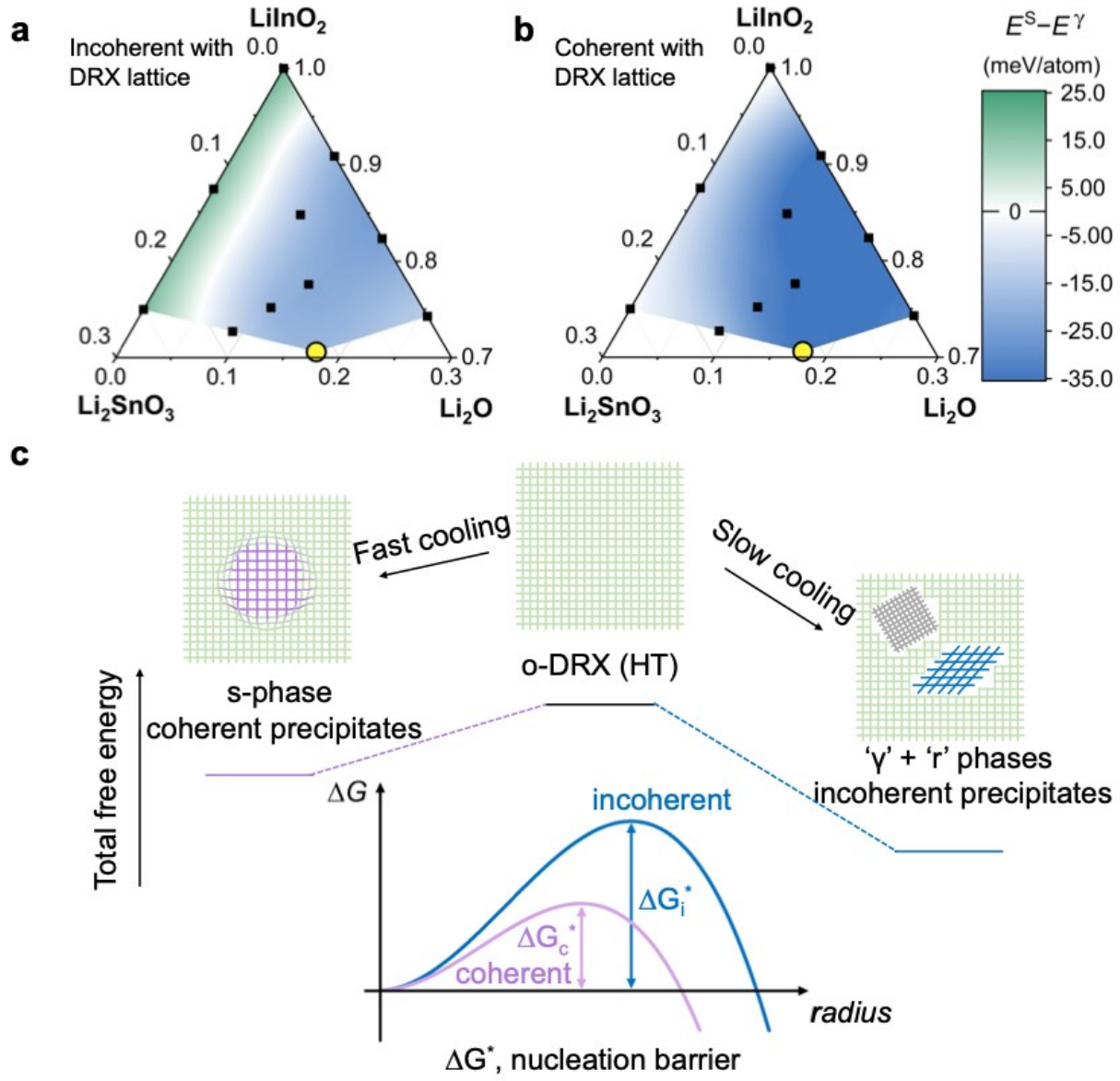

Figure 5. Kinetically driven s-phase formation through coherent precipitation. Calculated and interpolated relative energy difference (at 0 K) between s-phase and 'γ' phase structures when they are **(a)** fully relaxed by DFT to simulate incoherent precipitation and **(b)** confined by the average o-DRX lattice parameter to simulate coherent precipitation. The black square denotes the DFT-computed over-stoichiometric Li–In–Sn–O compositions and the yellow circle denotes the $Li_{17}In_9SnO_{24}$ (L17) composition. More negative $E^S - E^\gamma$ values are represented by deeper blue colors, and more positive $E^S - E^\gamma$ values are represented by deeper green colors. The white color

denotes a relative energy difference of 0 meV/atom. **(c)** Schematic illustrations of energetics and nucleation barriers of coherent and incoherent precipitates formed during fast and slow cooling, respectively. The o-DRX, s-phase, 'γ' and 'r' phases are colored green, purple, grey, and blue, respectively.

Improved Li-ion conductivity through low-temperature re-annealing

To further improve the Li-ion conductivity of o-LISO, we attempted to increase the phase fraction of the s-phase. In principle, this increase can be achieved by controlling the cooling rate to be moderate, not too fast so that the s-phase has sufficient time to nucleate and grow, and not too slow to avoid phase decomposition. However, in reality, it is challenging to regulate the cooling rate to a value between air quenching and natural cooling. Instead, we attempted a low-temperature post-annealing process for air-quenched o-LISO to promote s-phase growth.

To identify the appropriate temperature for post-annealing treatment, we reannealed o-LISO at 400 °C, 500 °C, and 800 °C and monitored the phase evolutions. As shown in Figure S7, reannealing at 400 °C for 24 h preserves the s-phase and o-DRX without any phase decomposition. However, after reannealing at 500 °C for 24 h, we observed the formation of a small amount of 'γ' and 'r' phases in the XRD pattern, indicating that phase decomposition starts to occur at this temperature. After reannealing at 800 °C for only 1 h, the sample fully decomposed into 'γ' and 'r' phases. A post-annealing temperature of 400 °C was thus selected as it is the highest temperature tested that avoids phase decomposition. The XRD pattern of o-LISO reannealed at 400 °C for 1 month, shown in Figure S8, still exhibits the s-phase alongside the o-DRX phase, confirming that no phase decomposition occurred during this process. Elemental analysis performed by inductively coupled plasma mass spectroscopy (ICP-MS) confirmed that the Li

content in pristine o-LISO (Li: In: Sn = 15.2: 9.0: 1) is similar to that in o-LISO reannealed at 400 °C for 1 month (Li: In: Sn = 15.5: 8.8: 1) (Table S2), which is also consistent with o-LISO composition reported in the previous study[17]. This suggests that post-annealing at 400 °C does not cause noticeable Li loss from the material.

EIS measurements were performed to probe the Li-ion conductivity of o-LISO that has undergone a post-annealing treatment. Figure 6a presents Nyquist plots of pristine o-LISO and o-LISO reannealed at 400 °C for 5 days and for 1 month. After reannealing for 5 days, the RT Li-ion conductivity increases to 8.08×10^{-4} S cm^{-1}, which is double that of the pristine o-LISO (4.09×10^{-4} S cm^{-1}). Lengthening the annealing time to 1 month leads to a further increase in ionic conductivity, as indicated by the Nyquist plot, which now displays two distinct semicircles (Figure 6a). The impedance spectrum of o-LISO reannealed for 1 month was fit with an equivalent circuit consisting of two parallel constant phase elements (CPE) /resistors (R) in series with a further CPE, as shown in Figure S9. The capacitance of the high-frequency CPE1/R1 elements is 3.06×10^{-9} F, which implies both grain and grain boundary contributions to the impedance response[27]. While the capacitance of the intermediate-frequency CPE2/R2 elements is 3.03×10^{-7} F, which can be attributed to a surface layer between the sample pellet and In electrode[27]. Thus, the resistance of R1 was used to calculate the total ionic conductivity of o-LISO reannealed for 1 month, which reaches 1.45×10^{-3} S cm^{-1} at RT. Therefore, the low-temperature post-annealing treatment indeed improves the ionic conductivity, which approaches the calculated value of the pure s-phase (3.17×10^{-3} S cm^{-1})[17]. Variable temperature EIS was applied to probe the activation energy of Li-ion conduction, with the Arrhenius plots shown in Figure 6b. The results indicate that o-LISO reannealed at 400 °C has a similar activation energy (258 meV and 245 meV for samples reannealed for 5 days and 1 month, respectively) as pristine o-LISO (255 meV), whereas the pre-

factor increases with longer reannealing time. This is expected because the Li-ion conduction mechanisms in 400 °C-reannealed o-LISO and pristine o-LISO are the same, consisting of Li-ion migration through the Tet–Oct face-sharing pathways. The increase in the pre-factor may suggest that 400 °C-reannealed o-LISO has a larger fraction of s-phase domains or better-connected domains than the pristine sample. In Figure 6c, We compare EIS-measured ionic conductivity and activation energy with other reported oxide-based Li superionic conductors including Garnets, NASICONs, perovskites, LISICONs, etc[28-40]. o-LISO reannealed at 400 °C for 1 month (red star) exhibits a higher ionic conductivity with a lower activation energy than most oxides.

To better understand the effect of 400 °C post-annealing on the Li environment in o-LISO, we collected the ^{6}Li ssNMR spectrum on o-LISO reannealed for 1 month, with the results shown in Figure 6d. Compared to pristine o-LISO, the broad resonance in the spectrum of the 400 °C-reannealed o-LISO is displaced to a higher chemical shift, from 7.6 to 9.3 ppm. As discussed in the previous section (Figure 2b), the broad signal in the ^{6}Li ssNMR spectrum corresponds to Tet Li and requires a two-component model fit, with the component at the higher chemical shift (9.5 ppm) being mainly associated with Tet Li in the s-phase. We used the same two-component model to fit the broad signal in the spectrum of 400 °C-reannealed o-LISO. The fitting clearly shows a significant change in the ratio of the two components that describe the broad resonance. After 1 month of reannealing, the component with the higher chemical shift (purple shading) increases significantly and becomes the major contributor to the broad-resonance line shape, whereas the lower-chemical-shift component (green shading) decreases compared with that in the pristine o-LISO (Figure 6d and Table S1). This observation is consistent with our hypothesis that 400 °C-reannealed o-LISO has a larger fraction of s-phase domains than pristine o-LISO, thereby leading to a higher ionic conductivity. We note that the XRD patterns (Figure S8) do not reveal significant

differences in the s-phase domains after reannealing. This is probably because XRD provides bulk-averaged data and is not sensitive enough to detect changes in phase distribution within the microstructure. Advanced electron microscopy techniques would be necessary to probe the microstructure and quantify domain growth during 400 °C annealing, which needs further study.

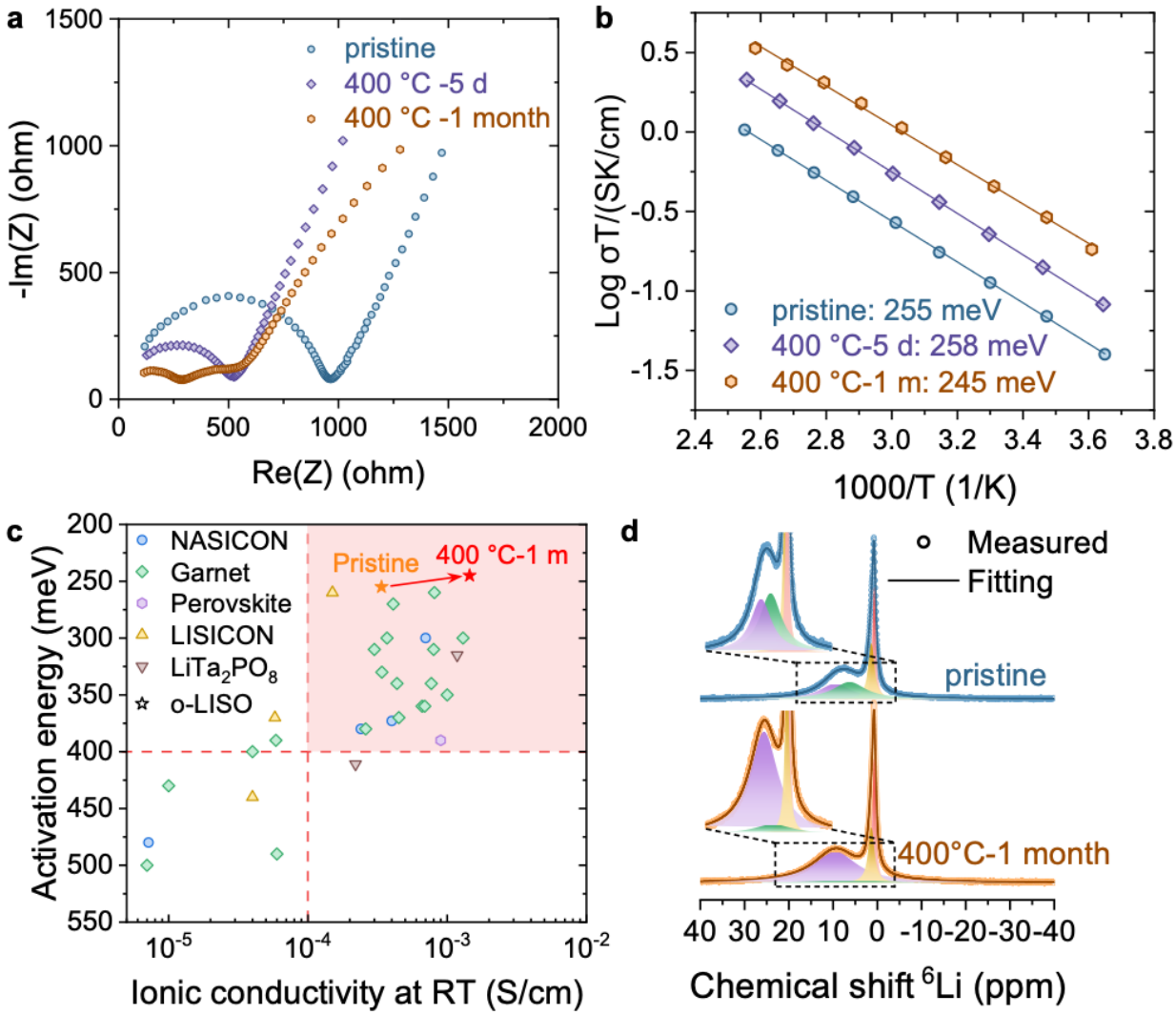

Figure 6. Li-ion conductivity and structural characterization of o-LISO with post-annealing treatment. (a) RT Nyquist plots of pristine o-LISO (without post-annealing treatment) and o-LISO reannealed at 400 °C for 5 days and for 1 month. **(b)** Arrhenius plots of Li-ion conductivities in the temperature range from 0 °C to 120 °C for pristine o-LISO and o-LISO reannealed at 400 °C

for 5 days and for 1 month. **(c)** Ionic conductivity and activation energy of o-LISO (both pristine and reannealed at 400 °C for 1 month) versus known oxide-based solid-state Li conductors (experimental reports)[28-40]. The red-shaded region highlights superionic conductors, which typically have room-temperature ionic conductivities higher than 10^{-4} S cm^{-1} and activation energies for ion conduction lower than 400 meV. **(d)** ^{6}Li MAS ssNMR spectra of pristine o-LISO and o-LISO reannealed at 400 °C for 1 month. The fitting components are shown in colored shadings.

Discussion

Although a single-phase material with a homogeneous microstructure is ideal to study for certain properties, in some cases, multi-phase materials inevitably form and possess attractive properties that allow them to be applied in many fields, such as metal-alloy hardening[41], piezoelectricity[42], and energy storage[43-44]. Nevertheless, engineering multi-phase materials is in general much more intricate than that of single-phase materials due to the inherent variety of microstructures. To achieve fine control over the microstructure and optimize the properties of multi-phase materials, it is vital to understand the synthesis mechanism that governs the formation as well as the evolution of those phases.

o-LISO, a recently reported Li superionic conductor, is a multi-phase system with a nanosized s-phase embedded in the o-DRX matrix[17]. By combining ex situ and in situ XRD experiments, we observed several phases including o-DRX, s-phase, 'γ' and 'r' phases that form under different conditions. Our ab initio calculations indicate that with low-to-intermediate levels of Li over-stoichiometry, the s-phase is the most stable at low temperature if phase separation into phases with different compositions can be prevented. At high temperature (e.g., 1050 °C), o-DRX can be

stabilized due to its large configurational entropy. This temperature-dependent stability steers cation ordering from a disordered state (o-DRX) to a spinel-like partially ordered state (s-phase) upon cooling. This s-phase is metastable at low temperature against decomposition into the 'γ' phase, with stoichiometric Li, and the 'r' phase, which can accommodate a high Li content by ordering Li into edge-sharing tetrahedral dumbbells. The phase separation into 'γ' and 'r' phases avoids the high-energy face-sharing configurations that exist in o-DRX or the s-phase and is thus more thermodynamically favorable. As a result, during slow cooling, the 'γ' and 'r' phases form from o-DRX instead of the s-phase.

Fast cooling can prevent phase separation into 'γ' and 'r' as long range diffusion is required to form these phases with compositions different from the parent o-DRX. This leaves as only option a transformation from o-DRX to s-phase which only requires rearrangement of the face-sharing tetrahedral units and is nominally at constant composition. The transformation from o-DRX to s-phase may be further favored by its reasonable lattice match which allows coherent precipitation as shown by our STEM analysis presented in Figure 4. The limited time during fast cooling for the s-phase to nucleate and grow results in its nanosized domain microstructure in the DRX matrix, as observed in our previous study[17]. Although the s-phase forms in the final product with fast cooling, upon reheating to high temperatures, the phases decompose into the 'γ' and 'r' phases again, which subsequently reform into the o-DRX phase when temperature is above 1000 °C, as shown in Figure S10. This result further supports the metastable nature of the s-phase.

The transition from o-DRX to the s-phase can be thought of as a metastable order-disorder transition which occurs when the decomposition into the stable equilibrium formed by 'γ' and 'r' can be prevented. Therefore, we identify coherent precipitation as the key mechanism for s-phase formation in the o-LISO system. Although the metastable s-phase cannot be thermodynamically

stabilized in any temperature range, i.e., the s-phase cannot form by simply heating to a specific temperature, it is kinetically accessible by controlling the cooling rate. Indeed, this coherent precipitation mechanism has been discovered and studied in many other multi-phase systems, e.g., coherent precipitation strengthening in intermetallic compounds like Al-Cu alloys[45-47] and hardening in alkaline niobate ferroelectrics[48]. In this study, we demonstrate that coherent precipitation can be used to stabilize high-energy cation configurations to achieve high Li-ion conductivity.

It is likely that we have not yet identified the ideal cooling profile that would maximize the fraction of s-phase in the sample. Such a temperature-time profile would have to maximize s-phase growth while preventing nucleation of 'γ' or 'r'. Such optimized annealing treatments are well known in steel making and other metallurgical processes but are not common to the field of solid-state electrolytes. It is also possible that some extreme conditions like high pressure[49] may stabilize the metastable s-phase in this ORX system, which needs to be further investigated. By applying a simple 400 °C post-annealing treatment, we were able to further improve the RT Li-ion conductivity of o-LISO to 1.45×10^{-3} S cm^{-1}. This makes o-LISO one of the fastest Li-ion conductors among oxides. We expect that this approach can be utilized generally to improve the ionic conductivities of ORX compounds.

This work sheds further light on the stabilization of face-sharing configurations in general ORX materials. Taking o-LISO as an example, the spinel-like ordering in the s-phase guarantees that Tet Li induced from Li over-stoichiometry only face-shares with Li instead of with high-valent cations, which stabilizes it at low temperature over the disordered state. At the same time, the s-phase, forming as kinetically favorable coherent precipitates, avoids direct phase decomposition of high-temperature o-DRX into 'γ' and 'r' phases and thus kinetically traps the system in a

metastable state where face-sharing configurations are conserved. This leads to synthetic accessibility of ORX materials with face-sharing configurations, which enables fast Li-ion conduction.

In summary, we systematically explored the phase-formation mechanism in a prototypical ORX compound, o-LISO. We found that the s-phase forms as nanosized domains from o-DRX upon fast cooling. This behavior can be rationalized by the fact that the s-phase is a thermodynamically metastable yet kinetically favorable phase upon cooling from o-DRX owing to the coherent precipitation. We identify the s-phase as the key to ORX system because: 1) the spinel-like cation ordering in the s-phase can better stabilize the face-sharing configurations induced by Li over-stoichiometry; 2) the s-phase forming as coherent precipitates can avoid direct phase decomposition and kinetically trap the metastable face-sharing configurations; and 3) the s-phase exhibits a high ionic conductivity due to the fully 3D-connected face-sharing Li pathways. With this understanding, we further improved the Li-ion conductivity of o-LISO to above 1 mS cm^{-1} by applying a post-annealing treatment. Our work provides a good example of comprehending the synthesis mechanism of multi-phase materials to achieve rational optimization of material properties.

Methods

Synthesis: o-LISO was synthesized using a traditional solid-state method. Li_2CO_3 (Alfa Aesar, ACS, 99%min), In_2O_3 (Sigma-Aldrich, 99.998%), and SnO_2 (Sigma-Aldrich, 99.9%) were used as precursors. The precursors were stoichiometrically mixed in ethanol (except that 10% excess

Li_2CO_3 was added to compensate for the Li loss during synthesis) in a 50-mL stainless-steel jar with five 10-mm-diameter stainless-steel balls using a Retsch PM200 planetary ball mill at 250 rpm for 12h. The precursors were then dried overnight in a 70 °C oven and pelletized. The precursor pellets were placed in an Al_2O_3 crucible and calcined in air at 1050 °C for 4 h and then air-quenched to room temperature. After the calcination, the pellets were manually ground into powders and shaker-milled for 30 min in air using a SPEX 8000M mixer/mill to decrease the particle size. The resulting powders were pelletized and sintered in air again at 1050 °C for 6 h to densify the pellets. The sintered pellets were air-quenched to room temperature and transferred to a glovebox for further study. The calcination and sintering times must be well controlled to ensure the appropriate amount of Li loss, and they can be dependent on the furnace as this affects the Li-loss rate. The key is to always add some excess Li precursors (e.g., 10%) at the beginning and to use the heat-treatment time to control the Li loss to the desired amount, leading to a final composition of approximately $Li_{15}In_9SnO_{23}$. For example, for o-LISO, we aimed to achieve the Li content at which the DRX and s-phase appeared without the Li_3InO_3-like phase. For the synthesis of WQ-o-LISO, a platinum crucible was used as the sample container instead of an Al_2O_3 crucible during calcination and sintering, and a water quench was applied by quickly removing the crucible from the furnace at 1050 °C and placing it upright in ice water, ensuring that the water level remained below the crucible's opening to prevent the sample from being immersed. For liquid nitrogen quench, a platinum crucible was used as the sample container and the crucible was quickly removed from the furnace at 1050 °C and placed it in liquid nitrogen. For the 400 °C post-annealing treatment, the sintered air-quenched o-LISO pellets were placed in an Al_2O_3 crucible and annealed at 400 °C.

Lab-based characterization: The lab XRD patterns of the as-synthesized compounds were obtained using a Rigaku MiniFlex 600 diffractometer equipped with a Cu source. The TGA and DSC measurements were performed using a SDT Q600 system (TA Instruments): 20 mg of mixed precursor powders were heated from room temperature to 1050 °C at a heating rate of 5 °C min^{-1} under O_2 flow.

Conductivity measurements: The Li-ion conductivities were evaluated using EIS with indium metal as the ion-blocking electrodes at temperatures ranging from 0 °C to 120 °C. The sintered pellets (at ~90%−95% relative density) were first polished with sandpaper to remove the surface layer that had severe Li loss and were then sandwiched between two indium films. The pellets with indium films were pressed using cold isostatic pressing (MTI, YLJ-CIP-20B) at 35 MPa for 30 min to ensure good contacts between the indium films and the pellet and then transferred into Bio-Logic Leak-tight sample holders (CESH) for the EIS measurements. The EIS measurements were performed using an EC-Lab Electrochemistry VMP300 (Bio-Logic) in the frequency range of 7 MHz to 100 mHz with a 10-mV voltage amplitude. A Bio-Logic intermediate temperature system was used to control the temperature of the sample holder.

In situ synchrotron XRD experiment: The in situ XRD was conducted at beamline 28-ID-2 of the National Synchrotron Light Source II (NSLS-II) at Brookhaven National Laboratory. The precursor materials were compacted into pellets, loaded into a Linkam furnace (model TS1500), and attached to the beamline setup. The Linkam furnace, equipped with temperature control, enabled X-ray transmission while maintaining a stable temperature environment. The sample was initially heated to 600 ℃ and then to 1050 ℃ at heating rates of 20 ℃/min and 10 ℃/min,

respectively. After heating, the sample was held at 1050 °C for 1 h. Subsequent cooling was performed at a rate of 100 ℃/min for rapid cooling. During the in situ experiment, XRD patterns were continuously recorded every minute: each pattern consists of 10 frames with an exposure time of 3 second per frame, totaling 30 seconds of acquisition time, followed by a 30-second interval before the next collection.

TEM characterization: TEM samples of o-LISO particles were prepared by dispersing them onto TEM lacey carbon grids inside an Ar-filled glovebox. High-angle annular dark field (HAADF) imaging was conducted using a Spectra Ultra microscope equipped with an aberration corrector operating at 300 kV. During imaging, a convergence angle of 30 mrad and collection angles of 60 to 180 mrad were used. To prevent beam-induced alterations, a probe current of 25 pA was used throughout the imaging process.

ssNMR spectroscopy: ^{6}Li solid-state NMR (ssNMR) spectra were recorded at B_0= 9.4 T (400.1 MHz for ^{1}H) using a Bruker BioSpin spectrometer equipped with an AVANCE NEO console and a 3.2 mm double resonance HX magic angle spinning (MAS) probe tuned to ^{6}Li (100.6 MHz). Samples were loaded in thin wall 3.2 mm zirconia rotors, closed using Vespel® caps, and spun at the magic angle at ν_R = 20 kHz using dry nitrogen. ^{6}Li chemical shift was externally referenced to a 1M aqueous solution of LiCl (δ_{iso}(^{6}Li) = 0 ppm). ^{6}Li ssNMR spectra were obtained using a rotor synchronized spin-echo sequence (90° − τ_R − 180° − τ_R – AQ) with a 90° radio frequency (RF) pulse of 10.9 μs, equivalent to an RF-field of 22.9 kHz. For quantitative ^{6}Li spin-echo spectra (τ_R = 1 rotor period), a total of 512 transients were averaged using a repetition time of

1 s, which was long enough to reach full relaxation of all the ^{6}Li signals of the samples. All solid-state NMR data were processed using Bruker TopSpin 4.2.0 and fitted using DMfit software[50].

ICP-MS: Elemental analysis for o-LISO samples were performed using inductively coupled plasma mass spectroscopy (Agilent 7900). Around 3 mg powder sample was added to a 20 mL vial, following by adding 12 mL aqua regia (a mixture of 3 mL concentrated nitric acid and 9 mL concentrated hydrochloric acid). The solution was diluted to ca. 150 ppb for each element with 5% nitric acid solution after all the powder was dissolved. The calibration curve was generated using standard solutions with 5 different concentrations ranging from 1 ppb to 1000 ppb. Linear fitting was applied.

DFT calculations: First-principles density-functional theory (DFT) calculations were performed to obtain an accurate description of the total energy of the Li–In–Sn–O (LISO) solid-electrolyte materials involved in this study. All the calculations were performed using the projector-augmented wave (PAW) method as implemented in the Vienna ab initio Simulation Package (VASP)[51]. The meta-GGA functional r^{2}SCAN was used to obtain more accurate description of the phase stability[52-53]. For all calculations, a reciprocal space discretization of 25 K-points per $Å^{-1}$ was applied, and the convergence criteria were set as 10^{-6} eV for electronic loops and 0.02 eV/Å for ionic loops. All calculations were performed with spin-polarization and initialized in a ferromagnetic spin state.

For the high-throughput stability-diagram calculations, for each LISO composition, four types of cation ordering were considered: spinel-like ordering (s-phase, Fd-3m), disordered-rocksalt-like ordering (o-DRX, Fm-3m), $LiInO_2$-type ordering ('γ', $I4_1/amd$), and Li_3InO_3-like

ordering ('r', P-3m1). For each type of ordering, we computed the Ewald summation and enumerated 10 configurations with low electrostatic energy for DFT calculation[19]. The thermodynamic stability of the s-phase LISO compositions was evaluated by constructing a convex hull of the DFT total energy relative to all competing phases in the chemical space available in the Materials Project (MP) database[20-21, 54]. The convex hull ensures that each ground state has an energy lower than any linear combination of phases that leads to the same composition as the ground state. The phase stability for s-phase compositions not on the hull is quantified by their energy above the hull (E_{hull}), which indicates the driving force of the compound for decomposition into other ground states. E_{hull} serves as a reasonable indicator of synthetic accessibility, as experimentally accessible materials generally have a low E_{hull}[54].

To predict relative stability of each phase at elevated temperatures, we added the entropy of ideal mixing to the DFT-computed energies. The entropy of ideal mixing is evaluated based on the level of cation disorder on specific crystallographic sites, which are different for all four phases. We normalized the DFT energies by a per-O_4 basis. The site multiplicities (m) and cation disorder in each phase are listed as follows (per O_4):

Phase	s-phase (O on 32e)	d-phase (O on 4b)	γ-phase (O on 8e)	r-phase (O on 2d)
Disordered site (m per O_4): species	8a (1): Li/vacancy	8c (8): Li/vacancy	16g (8): Li/vacancy	2d (4): Li/vacancy
	16d (2): Li/In/Sn	4a (4): Li/In/Sn	4a (2): Li/In/Sn	1b (2): In/Sn/vacancy

Based on the multiplicity table above, the entropy of ideal mixing on a per-O_4 basis for each phase was calculated using the following equation:

$$S_i = k_B \sum_j m_j \left[x_j \ln(x_j) + (1 - x_j) \ln(1 - x_j)\right],$$

where *i* refers to a specific phase and *j* refers to a specific species partially occupying a given site. Here, x_j are normalized by the total number of its given site present in the structure.

In the lattice-parameter constrained energy calculation for simulating variations of s-phase relative stability with the 'γ' phase under the scenario of coherent precipitation, we focused on the $LiInO_2$–Li_2SnO_3–Li_2O ternary diagram in the vicinity of $Li_{17}In_9SnO_{24}$ and selected compositions that allow us to construct a common supercell for all four phases. To obtain a reasonable starting structure for the o-DRX phase, for each considered composition, we enumerated 10 structures with low Ewald energy and performed DFT relaxations for each. The relaxed lattice parameters were averaged to obtain a representative o-DRX structure for each composition. To gauge incoherent precipitation, the s-phase and 'γ' phase structures (each composition also contains 10 configurations) were fully relaxed starting from the average o-DRX lattice. To simulate coherent precipitation, we instead performed a volume-invariant relaxation on the s-phase and 'γ' phase structures based on the average o-DRX lattice parameters, which only allows atoms to move within the cell of a given o-DRX structure.

Supporting Information

Supporting Information is available from the Wiley Online Library or from the author.

Acknowledgements

This work was supported by the Assistant Secretary for Energy Efficiency and Renewable Energy, Vehicle Technologies Office, of the U.S. Department of Energy under Contract No. DE-AC02-05CH11231. This work used the 28-ID-2 (XPD) beamline of the National Synchrotron Light Source II (NSLS-II), a US Department of Energy (DOE) Office of Science User Facility operated for the DOE Office of Science by Brookhaven National Laboratory under contract No. DE-SC0012704. The TEM work was carried out by using the microscopes that are funded in part by a grant from the Washington State Department of Commerce's Clean Energy Fund. The work was conducted at the Environmental Molecular Sciences Laboratory (EMSL), a national scientific user facility sponsored by the DOE's Office of Biological and Environmental Research and located at PNNL. PNNL is operated by Battelle for the U.S. DOE under the Contract DE-AC05- 76RL01830. We thank Drs. Hasan Celik, and UC Berkeley's NMR facility in the College of Chemistry (CoC-NMR) for spectroscopic assistance. The instrument used in this work is supported by the National Science Foundation under Grant No. 2018784. Research at Argonne National Laboratory is supported by the U.S. Department of Energy Office of Energy Efficiency and Renewable Energy Vehicle Technologies Office under Contract No. DEAC02-06CH11357. The computational analysis was performed using computational resources sponsored by the DOE's Office of Energy Efficiency and Renewable Energy and located at the National Renewable Energy Laboratory. Computational resources were also provided by the Extreme Science and Engineering Discovery Environment (XSEDE), supported by National Science Foundation grant number ACI1053575, and the National Energy Research Scientific Computing Center (NERSC), a DOE Office of Science User Facility supported by the Office of Science and the U.S. Department of Energy under Contract No. DE-AC02-05CH11231. This research also used the Lawrencium computational

cluster resource provided by the IT Division at Lawrence Berkeley National Laboratory (Supported by the Director, Office of Science, Office of Basic Energy Sciences of the U.S. Department of Energy under contract no. DE-AC02-05CH11231).

Conflict of Interest

The authors declare no conflict of interest.

References

[1] M. Bianchini, J. Wang, R. J. Clement, B. Ouyang, P. Xiao, D. Kitchaev, T. Shi, Y. Zhang, Y. Wang, H. Kim, M. Zhang, J. Bai, F. Wang, W. Sun, G. Ceder, *Nat Mater* **2020**, 19, 1088.
[2] Z. J. Cai, Y. Q. Zhang, Z. Y. Lun, B. Ouyang, L. Gallington, Y. Z. Sun, H. M. Hau, Y. Chen, M. C. Scott, G. Ceder, *Advanced Energy Materials* **2022**, 12, 2103923.
[3] M. J. McDermott, B. C. McBride, C. E. Regier, G. T. Tran, Y. Chen, A. A. Corrao, M. C. Gallant, G. E. Kamm, C. J. Bartel, K. W. Chapman, P. G. Khalifah, G. Ceder, J. R. Neilson, K. A. Persson, *ACS Central Science* **2023**, 9, 1957.
[4] Y. Chen, E. Rangasamy, C. R. dela Cruz, C. Liang, K. An, *Journal of Materials Chemistry A* **2015**, 3, 22868.
[5] D. P. Shoemaker, Y.-J. Hu, D. Y. Chung, G. J. Halder, P. J. Chupas, L. Soderholm, J. F. Mitchell, M. G. Kanatzidis, *Proceedings of the National Academy of Sciences* **2014**, 111, 10922.
[6] A. J. Martinolich, J. R. Neilson, *Chemistry of Materials* **2017**, 29, 479.
[7] P. K. Todd, M. J. McDermott, C. L. Rom, A. A. Corrao, J. J. Denney, S. S. Dwaraknath, P. G. Khalifah, K. A. Persson, J. R. Neilson, *Journal of the American Chemical Society* **2021**, 143, 15185.
[8] A. Miura, C. J. Bartel, Y. Goto, Y. Mizuguchi, C. Moriyoshi, Y. Kuroiwa, Y. Wang, T. Yaguchi, M. Shirai, M. Nagao, N. C. Rosero-Navarro, K. Tadanaga, G. Ceder, W. Sun, *Advanced Materials* **2021**, 33, 2100312.
[9] Z. Jiang, A. Ramanathan, D. P. Shoemaker, *Journal of Materials Chemistry C* **2017**, 5, 5709.
[10] K. Mizushima, P. C. Jones, P. J. Wiseman, J. B. Goodenough, *Materials Research Bulletin* **1980**, 15, 783.
[11] J. Lee, A. Urban, X. Li, D. Su, G. Hautier, G. Ceder, *Science* **2014**, 343, 519.
[12] M. M. Thackeray, P. J. Johnson, L. A. de Picciotto, P. G. Bruce, J. B. Goodenough, *Materials Research Bulletin* **1984**, 19, 179.
[13] K. M. Shaju, P. G. Bruce, *Dalton Transactions* **2008**, 5471.

[14] H. Liu, Z. Zhu, Q. Yan, S. Yu, X. He, Y. Chen, R. Zhang, L. Ma, T. Liu, M. Li, R. Lin, Y. Chen, Y. Li, X. Xing, Y. Choi, L. Gao, H. S. Cho, K. An, J. Feng, R. Kostecki, K. Amine, T. Wu, J. Lu, H. L. Xin, S. P. Ong, P. Liu, *Nature* **2020**, 585, 63.
[15] X. Guo, C. Chen, S. P. Ong, *Chemistry of Materials* **2023**, 35, 1537.
[16] H. Ge, N. Li, D. Li, C. Dai, D. Wang, *The Journal of Physical Chemistry C* **2009**, 113, 6324.
[17] Y. Chen, Z. Lun, X. Zhao, K. P. Koirala, L. Li, Y. Sun, C. A. O'Keefe, X. Yang, Z. Cai, C. Wang, H. Ji, C. P. Grey, B. Ouyang, G. Ceder, *Nat Mater* **2024**, 23, 535.
[18] J. J. De Yoreo, P. G. Vekilov, *Reviews in Mineralogy and Geochemistry* **2003**, 54, 57.
[19] A. Y. Toukmaji, J. A. Board, *Computer Physics Communications* **1996**, 95, 73.
[20] S. P. Ong, L. Wang, B. Kang, G. Ceder, *Chemistry of Materials* **2008**, 20, 1798.
[21] A. Jain, S. P. Ong, G. Hautier, W. Chen, W. D. Richards, S. Dacek, S. Cholia, D. Gunter, D. Skinner, G. Ceder, K. A. Persson, *APL Materials* **2013**, 1, 011002.
[22] S. P. Ong, A. Jain, G. Hautier, B. Kang, G. Ceder, *Electrochemistry Communications* **2010**, 12, 427.
[23] V. I. Kalikmanov, in *Nucleation Theory*, (Ed: V. I. Kalikmanov), Springer Netherlands, Dordrecht 2013.
[24] D. A. Porter, K. E. Easterling, *Phase transformations in metals and alloys (revised reprint)*, CRC press, **2009**.
[25] A. Navrotsky, L. Mazeina, J. Majzlan, *Science* **2008**, 319, 1635.
[26] S. Sakurai, A. Namai, K. Hashimoto, S.-i. Ohkoshi, *Journal of the American Chemical Society* **2009**, 131, 18299.
[27] I. M. Hodge, M. D. Ingram, A. R. West, *Journal of Electroanalytical Chemistry and Interfacial Electrochemistry* **1976**, 74, 125.
[28] H. Aono, N. Imanaka, G.-y. Adachi, *Accounts of chemical research* **1994**, 27, 265.
[29] J. Fu, *Solid State Ionics* **1997**, 104, 191.
[30] M. Illbeigi, A. Fazlali, M. Kazazi, A. H. Mohammadi, *Solid State Ionics* **2016**, 289, 180.
[31] H. Aono, E. Sugimoto, Y. Sadaoka, N. Imanaka, G.-y. Adachi, *Bulletin of the Chemical Society of Japan* **1992**, 65, 2200.
[32] L. Xiong, Z. Ren, Y. Xu, S. Mao, P. Lei, M. Sun, *Solid State Ionics* **2017**, 309, 22.
[33] Z. Zhang, Y. Shao, B. Lotsch, Y.-S. Hu, H. Li, J. Janek, L. F. Nazar, C.-W. Nan, J. Maier, M. Armand, L. Chen, *Energy & Environmental Science* **2018**, 11, 1945.
[34] J. Ibarra, A. Varez, C. León, J. Santamarıa, L. Torres-Martınez, J. Sanz, *Solid State Ionics* **2000**, 134, 219.
[35] D. Mazumdar, D. Bose, M. Mukherjee, *Solid state ionics* **1984**, 14, 143.
[36] G. Zhao, K. Suzuki, T. Okumura, T. Takeuchi, M. Hirayama, R. Kanno, *Chemistry of Materials* **2022**, 34, 3948.
[37] G. Zhao, K. Suzuki, T. Seki, X. Sun, M. Hirayama, R. Kanno, *Journal of Solid State Chemistry* **2020**, 292, 121651.
[38] J. Kuwano, A. West, *Materials Research Bulletin* **1980**, 15, 1661.
[39] Q. Wang, J. F. Wu, Z. Lu, F. Ciucci, W. K. Pang, X. Guo, *Advanced Functional Materials* **2019**, 29, 1904232.
[40] R. Kim, L. J. Miara, J. H. Kim, J. S. Kim, D. Im, Y. Wang, *Chemistry of Materials* **2021**, 33, 6909.
[41] P. Jacques, Q. Furnémont, A. Mertens, F. Delannay, *Philosophical Magazine A* **2001**, 81, 1789.

[42] C. Ma, H. Guo, S. P. Beckman, X. Tan, *Physical review letters* **2012**, 109, 107602.
[43] S. Li, S.-Q. Zhang, L. Shen, Q. Liu, J.-B. Ma, W. Lv, Y.-B. He, Q.-H. Yang, *Advanced Science* **2020**, 7, 1903088.
[44] L. Hu, J. Wang, K. Wang, Z. Gu, Z. Xi, H. Li, F. Chen, Y. Wang, Z. Li, C. Ma, *Nature Communications* **2023**, 14, 3807.
[45] A. Guinier, *Nature* **1938**, 142, 569.
[46] R. B. Nicholson, J. Nutting, *The Philosophical Magazine: A Journal of Theoretical Experimental and Applied Physics* **1958**, 3, 531.
[47] Q. Wang, Z. Li, S. Pang, X. Li, C. Dong, P. K. Liaw, *Entropy* **2018**, 20, 878.
[48] C. Zhao, S. Gao, H. J. Kleebe, X. Tan, J. Koruza, J. Rödel, *Advanced Materials* **2022**, 34, 2202379.
[49] M.-H. Zhao, C. Zhu, Z. Sun, T. Xia, Y. Han, Y. Zeng, Z. Gao, Y. Gong, X. Wang, J. Hong, W.-X. Zhang, Y. Wang, D.-X. Yao, M.-R. Li, *Chemistry of Materials* **2022**, 34, 186.
[50] D. Massiot, F. Fayon, M. Capron, I. King, S. Le Calvé, B. Alonso, J.-O. Durand, B. Bujoli, Z. Gan, G. Hoatson, *Magnetic Resonance in Chemistry* **2002**, 40, 70.
[51] G. Kresse, J. Furthmüller, *Computational Materials Science* **1996**, 6, 15.
[52] J. W. Furness, A. D. Kaplan, J. Ning, J. P. Perdew, J. Sun, *The journal of physical chemistry letters* **2020**, 11, 8208.
[53] R. Kingsbury, A. S. Gupta, C. J. Bartel, J. M. Munro, S. Dwaraknath, M. Horton, K. A. Persson, *Physical Review Materials* **2022**, 6, 013801.
[54] W. Sun, S. T. Dacek, S. P. Ong, G. Hautier, A. Jain, W. D. Richards, A. C. Gamst, K. A. Persson, G. Ceder, *Science Advances* **2016**, 2, e1600225.